A&A 639, A14 (2020)
https://doi.org/10.1051/0004-6361/202038015

Astronomy & Astrophysics

The Fornax Deep Survey with VST

VIII. Connecting the accretion history with the cluster density

M. Spavone[1], E. Iodice [1,2], G. van de Ven[3], J. Falcón-Barroso[4,5], M. A. Raj[1], M. Hilker[2], R. P. Peletier[6], M. Capaccioli[7], S. Mieske[8], A. Venhola[9], N. R. Napolitano[10], M. Cantiello[11], M. Paolillo[7,1,12], and P. Schipani[1]

[1] INAF-Astronomical Observatory of Capodimonte, Salita Moiariello 16, 80131 Naples, Italy
e-mail: marilena.spavone@inaf.it
[2] European Southern Observatory, Karl-Schwarzschild-Strasse 2, 85748 Garching bei Muenchen, Germany
[3] Department of Astrophysics, University of Vienna, Tuerkenschanzstrasse 17, 1180 Vienna, Austria
[4] Instituto de Astrofísica de Canarias, C/ Vía Láctea, s/n, 38205 La Laguna, Tenerife, Spain
[5] Departamento de Astrofísica, Universidad de La Laguna, 8200 La Laguna, Tenerife, Spain
[6] Kapteyn Astronomical Institute, University of Groningen, PO Box 72, 9700 Groningen, AV, The Netherlands
[7] University of Naples "Federico II", C.U. Monte Sant'Angelo, Via Cinthia, 80126 Naples, Italy
[8] European Southern Observatory, Alonso de Cordova 3107, Vitacura, Santiago, Chile
[9] Division of Astronomy, Department of Physics, University of Oulu, Oulu, Finland
[10] School of Physics and Astronomy, Sun Yat-sen University Zhuhai Campus, Daxue Road 2, 519082 Tangjia, Zhuhai, Guangdong, PR China
[11] INAF-Astronomical Abruzzo Observatory, Via Maggini, 64100 Teramo, Italy
[12] INFN, Sezione di Napoli, Napoli 80126, Italy

Received 24 March 2020 / Accepted 29 April 2020

ABSTRACT

Context. This work is based on deep multi-band (*g, r, i*) data from the Fornax Deep Survey with the VLT Survey Telescope (VST). We analyse the surface brightness profiles of the 19 bright early-type galaxies (ETGs; $m_B \leq 15$ mag) inside the virial radius of the Fornax cluster ($R_{\rm vir} \sim 0.7$ Mpc), in the mass range $8 \times 10^8 \leq M_* \leq 1.2 \times 10^{11}\ M_\odot$.
Aims. The main aim of this work is to identify signatures of accretion onto galaxies by studying the presence of outer stellar haloes and to understand their nature and occurrence. Our analysis also provides a new and accurate estimate of the intra-cluster light inside the virial radius of Fornax.
Methods. We performed multi-component fits to the azimuthally averaged surface brightness profiles available for all sample galaxies. This allows us to quantify the relative weight of all components in the galaxy structure that contribute to the total light. In addition, we derived the average $g - i$ colours in each component identified by the fit, as well as the azimuthally averaged $g - i$ colour profiles, to correlate them with the stellar mass of each galaxy and the location inside the cluster.
Results. We find that in the most massive ($10^{10} \leq M \leq 10^{11}\ M_\odot$) and reddest ETGs the fraction of light in, probably accreted, haloes (50%–90%) is much larger than in the other galaxies. All of these are located in the high-density region of the cluster ($\leq 0.4 R_{\rm vir} \sim 0.3$ Mpc), belonging to the north-south clump (NS clump). Less massive galaxies ($10^9 \leq M \leq 10^{10}\ M_\odot$) have an accreted mass fraction that is lower than 30%, have bluer colours, and reside in the low-density regions of the cluster. The colour profiles of the ETGs with the largest accreted mass fraction tend to flatten in the outskirts of the galaxy, that is beyond the transition radius from the central in situ to the ex situ accreted component. Inside the virial radius of the cluster (~0.7 Mpc), the total luminosity of the intra-cluster light, compared with the total luminosity of all cluster members (bright galaxies and dwarfs), is about 34%.
Conclusions. Inside the Fornax cluster there is a clear correlation between the amount of accreted material in the stellar haloes of galaxies and the density of the environment in which those galaxies reside. By comparing this quantity with theoretical predictions and previous observational estimates, there is a clear indication that the driving factor for the accretion process is the total stellar mass of the galaxy, which agrees with the hierarchical accretion scenario. Massive galaxies in the NS clump, with the largest accreted mass fractions, went through pre-processing in a group environment before this group merged with the main cluster early on. At the present epoch of the Fornax assembly history, these galaxies are the major contribution to the stellar density in the core of the cluster.

Key words. surveys – galaxies: elliptical and lenticular, cD – galaxies: fundamental parameters – galaxies: formation – galaxies: halos – galaxies: clusters: general

1. Introduction

Exploring the low surface brightness (LSB) universe is one of the most challenging tasks of the era of the deep imaging and spectroscopic surveys. It is a crucial ingredient to map the mass assembly of galaxies at all scales (from galaxies to clusters) and all environments (in groups of galaxies and in rich clusters), and to constrain their evolution within the Lambda-cold dark matter paradigm. Clusters of galaxies are expected to grow over time by accreting smaller groups. During the infall process, the material stripped from the galaxy outskirts builds up the intra-cluster light (ICL; see Napolitano et al. 2003; Contini et al. 2014, 2019; Cui et al. 2014; Pillepich et al. 2018; DeMaio et al. 2018; Henden et al. 2019). The ICL is the fossil record of all past interactions and mergers. It is a diffuse and typically very faint component ($\mu_g \geq 28$ mag arcsec^{-2}) that grows over time

with the infalling of galaxies in the potential well of the brightest cluster galaxy (BCG; Mihos 2015). The imprint of mass assembly in the BGGs resides in their extended stellar haloes. This is an extended (≥100 kpc; Pillepich et al. 2018) and faint ($\mu_g \geq 26$–27 mag arcsec^{-2}) component made of stars stripped from satellite galaxies, in the form of streams and tidal tails, with multiple stellar components and complex kinematics (see Duc et al. 2017; Mihos et al. 2017, for reviews).

Semi-analytic models combined with cosmological simulations give detailed predictions about the structure and stellar populations of stellar haloes, the ICL formation, and the amount of substructures in various kinds of environments (Oser et al. 2010; Cooper et al. 2013, 2015; Cook et al. 2016; Pillepich et al. 2018; Monachesi et al. 2019). New sets of simulations have recently been able to reproduce the faint features in galaxy outskirts at levels comparable to the deep observations (i.e. 29–33 mag arcsec^{-2}; Pop et al. 2018; Mancillas et al. 2019).

In the last two decades, deep imaging surveys enabled huge progress in the study of the mass assembly in different types of environments, by providing an extensive analysis of the light and colour distribution of galaxies out to the regions of stellar haloes and intra-cluster space (Ferrarese et al. 2012; van Dokkum et al. 2014; Duc et al. 2015; Munoz et al. 2015; Capaccioli et al. 2015; Trujillo & Fliri 2016; Merritt et al. 2016; Mihos et al. 2017; Iodice et al. 2016). Investigations of mass assembly in the outskirts of galaxies have also been conducted by means of stellar kinematics and population properties (e.g. Coccato et al. 2010, 2011; Ma et al. 2014; Barbosa et al. 2018; Veale et al. 2018; Hilker et al. 2018; Greene et al. 2019) and kinematics of discrete tracers such as globular clusters (GCs) and planetary nebulae (PNe; e.g. Coccato et al. 2013; Longobardi et al. 2013; Spiniello et al. 2018; Hartke et al. 2018; Prole et al. 2019; Napolitano et al. 2002; Pota et al. 2018). The main goal of the works cited above is to provide a set of observables that can be directly compared with theoretical predictions. For that, deep and large-scale multi-band imaging is required to (i) detect and characterise the substructures (like tidal tails or streams) in the stellar haloes, through morphology and colours; (ii) estimate the total accreted stellar mass by fitting the light distribution; and (iii) estimate the total luminosity of the ICL in the galaxy environment (i.e. group or cluster). Furthermore, deep spectroscopy in the galaxy outskirts is required to accurately constrain the age and metallicity of the stellar haloes.

Clusters and groups of galaxies are excellent sites to study the mass assembly and the build up of the ICL. The extensive multiwavelength observations available for the Fornax galaxy cluster made this target one of the best environments in which galaxy structure, stellar population, and LSB features, including the ICL, can be studied in great detail and used to trace the assembly history of the cluster (see Iodice et al. 2019b,a). Fornax is the second most massive galaxy concentration within 20 Mpc, after the Virgo cluster, and has a virial mass of $M_{\rm vir} = 7 \times 10^{13}\, M_\odot$ (Drinkwater et al. 2001).

In the optical wavelength range, *Hubble* Space Telescope (HST) data (Jordán et al. 2007), DECam data from the Next Generation Fornax Cluster Survey (Munoz et al. 2015), and the Fornax Deep Survey (FDS) with the VLT Survey Telescope (VST; Venhola et al. 2017; Iodice et al. 2016) are the deepest and widest datasets mapping the Fornax cluster out to the virial radius ($R_{\rm vir} \sim 0.7$ Mpc, Drinkwater et al. 2001). With FDS we (i) mapped the surface brightness around the BCGs NGC 1399 and NGC 1316 out to an unprecedented distance of about ∼200 kpc ($R \sim 6R_{\rm e}$) and down to $\mu_g \simeq 29$–31 mag arcsec^{-2} (Iodice et al. 2016, 2017b); (ii) traced the spatial distribution of candidate GCs inside a large fraction of the cluster core (D'Abrusco et al. 2016; Cantiello et al. 2018); (iii) studied the galaxy outskirts, detected ICL and faint ($\mu_g \simeq 28$–30 mag arcsec^{-2}) features in the intra-cluster region in the core of the cluster (Iodice et al. 2016, 2017a, 2019b; Raj et al. 2019) and in the outskirts of NGC 1316 (Iodice et al. 2017b); and (iv) provided the largest size and magnitude limited catalogue of dwarf galaxies in the cluster (Venhola et al. 2017, 2018).

The deep integral-field spectroscopic observations, provided by the Fornax3D (F3D) project (Sarzi et al. 2018; Iodice et al. 2019a) acquired with MUSE at the Very Large Telescope (VLT), give a complementary, unique, and complete dataset for the brightest galaxies ($m_B \leq 15$ mag) inside the virial radius of the Fornax cluster. In addition, new data from ALMA (Zabel et al. 2019), neutral hydrogen data from the MeerKAT survey (Serra et al. 2016) and integral field observations of dwarfs from the SAMI Fornax cluster dwarf galaxy survey (Scott et al. 2020) will provide a complete census of the cool interstellar medium in Fornax.

The wealth of data available for the Fornax cluster has confirmed that it has a complex structure, which is indicative of continuing mass assembly, previously suggested by Drinkwater et al. (2001) and Scharf et al. (2005). By combining the structural properties of the galaxies from FDS imaging with the spectroscopic data from F3D (i.e. morphology, colours, kinematics, and stellar population) in the two-dimensional projected phase-space, the cluster shows three well-defined groups of galaxies: the core, the north-south clump (NS clump), and the infalling galaxies (see Fig. 1), apart from the south-west merging group centred on NGC 1316 (Drinkwater et al. 2001). Galaxies in each group have different light and colour distributions, kinematics, and stellar populations properties (Iodice et al. 2019a).

The core is dominated by the brightest and massive cluster member NGC 1399, which is one of only two slow rotators inside the virial radius. This coincides with the peak of the X-ray emission (Paolillo et al. 2002).

The galaxies in the NS clump are the reddest and most metal-rich galaxies of the sample, have stellar masses in the range 0.3–$9.8 \times 10^{10}\, M_\odot$, and reside in the high-density region of the cluster (at a cluster-centre distance of $R_{\rm proj} \leq 0.4R_{\rm vir} \sim 0.3$ Mpc), where the X-ray emission is still detected (see Fig. 1). The bulk of the gravitational interactions between galaxies takes place in this region, where the intra-cluster baryons (i.e. diffuse light, GCs, and PNe) are found (Cantiello et al. 2018; Spiniello et al. 2018; Iodice et al. 2019b). All galaxies in the NS clump are fast-rotators early type galaxies (ETGs), many of which show distinct nuclear components and kinematically decoupled cores; two out of a total of three show ionised-gas emission in their centres. On average, galaxies populating this group show the largest differences between kinematic and photometric position angles. The stellar populations in the outskirts of galaxies in this clump have lower metallicity than the bright central regions, which is an indication that the mass assembly of metal-poor satellites has continued longer in the outskirts.

The infalling galaxies are distributed nearly symmetrically around the core in the low-density region of the cluster ($R_{\rm proj} \geq 0.4R_{\rm vir} \sim 0.3$ Mpc). The majority are late-type galaxies (LTGs) with ongoing star formation and signs of interaction with the environment and/or minor merging events in the form of tidal tails and disturbed molecular gas (Zabel et al. 2019; Raj et al. 2019). In this region, galaxies have on average lower [M/H] and [Mg/Fe] with respect to galaxies in the NS clump (Iodice et al. 2019a).

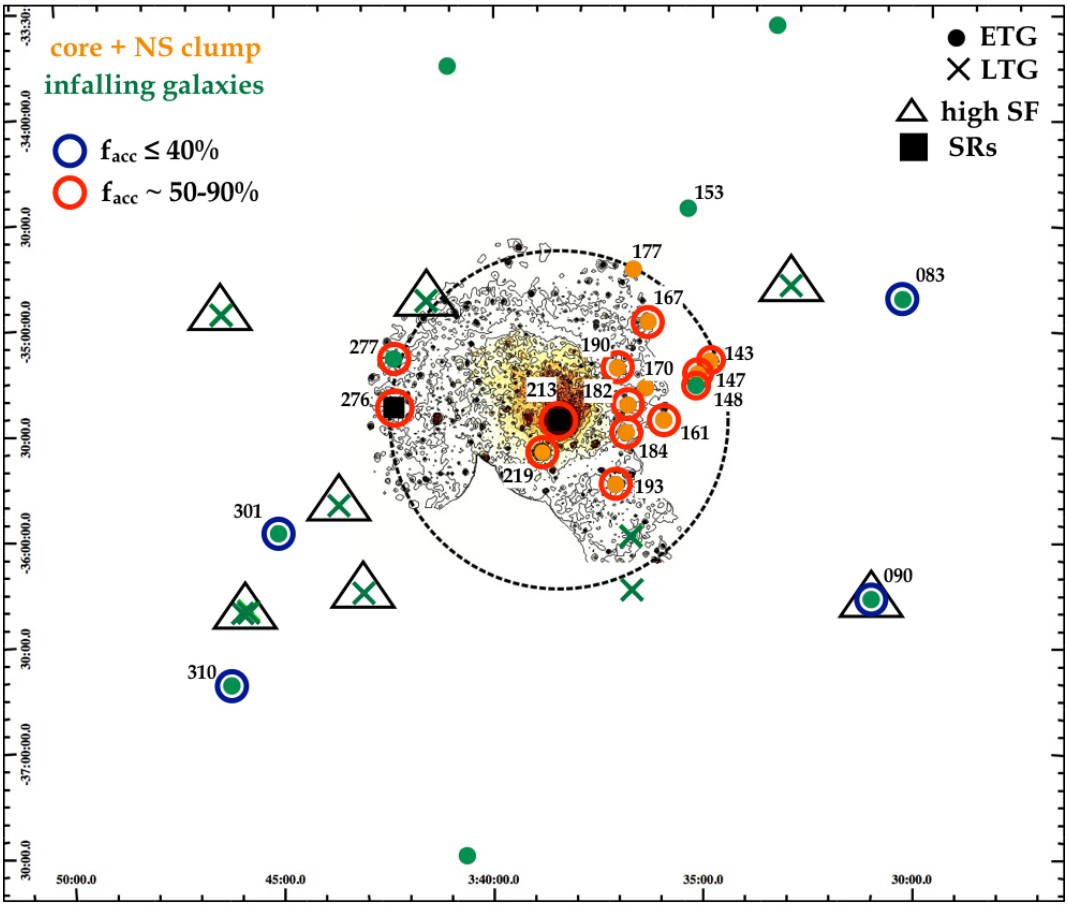

Fig. 1. Distribution of the brightest ($m_B \leq 16$ mag) ETGs (circles) and LTGs (crosses) of the Fornax cluster inside the virial radius, projected onto the sky plane. All ETGs studied in this paper are labelled with their FCC number (see Table 1). The right ascension and declination (J2000.0) are given in degrees on the horizontal and vertical axes of the field of view, respectively. The background image (and contours) is the X-ray emission in the energy range 0.4–1.3 KeV as measured by *XMM-Newton* (Frank et al. 2013). The dashed circle indicates the transition from the high-to-low density region of the cluster at 0.3 Mpc $\simeq 0.4\,R_{vir}$. The orange and green symbols represent the galaxies residing in the NS clump and the infalling galaxies, respectively (see text for details). Galaxies with high star formation (black open triangles) are also shown (Iodice et al. 2019a). The two slow rotators (SRs), FCC 213 and FCC 276, are denoted with black squares. Open blue and red circles indicate the fraction of the accreted mass estimated in this work. For the three edge-on lenticular galaxies FCC153, FCC170, FCC177 the accreted fraction could not be determined.

By exploiting the FDS images even further, in this work we add a new piece to the puzzle built above: we study the light and colour distribution of all brightest ETGs inside the viral radius of the Fornax cluster to constrain the accreted mass fraction as function of cluster density.

Theoretical predictions suggest that the brightest ETGs at the centre of groups and clusters are made by an inner stellar component formed in situ and an accreted ex situ component, which grows during the mass assembly. The ex situ component is comprised of a relaxed component, which is completely merged with the in situ component and an un-relaxed component, which is the outer stellar envelope. Simulations show that in the surface-brightness radial profile of simulated galaxies there is evidence of inflection in the region of the stellar haloes, corresponding to variations in the ratio of the accreted relaxed to the accreted un-relaxed components (Cooper et al. 2010; Deason et al. 2013; Amorisco 2017). This distance from the galaxy centre where the inflection occurs is the transition radius (R_{tr}) used to characterise stellar haloes. Massive galaxies with a high accreted mass fraction have small R_{tr} (Cooper et al. 2010, 2013). The un-relaxed component of the stellar envelope appears as a change in the slope at larger radii of the surface brightness profiles. In this context, the study of the surface brightness profiles of galaxies at the faintest levels is potentially one of the main tools available to quantify the contribution of the accreted mass, which becomes particularly efficient when the outer stellar envelope starts to be dominant beyond the transition radius (Iodice et al. 2016, 2017a, 2020; Spavone et al. 2017, 2018). To this aim, in this paper we used the *r*-band azimuthally averaged surface brightness profiles of ETGs inside the virial radius of the Fornax cluster (Iodice et al. 2019b) to perform a multi-component fit to estimate the relative contribution of the accreted component with respect to that formed in situ.

2. Data

The data used in this work are part of the FDS, which is a joint project based on guaranteed time observation of the FOCUS (P.I. R. Peletier) and VEGAS (P.I. E. Iodice, Capaccioli et al. 2015) surveys. Data from FDS consist of exposures in *u*, *g*, *r,* and *i* bands obtained with OmegaCAM at the VST (Schipani et al. 2012; Kuijken 2011), located at the European Southern Observatory in Cerro Paranal (Chile). Observations were acquired in visitor mode, dark time for the *u*, *g*, and *r* bands, and grey time for the *i* band. The FDS covers a 26 square degrees of the Fornax cluster, out to the virial radius ($R_{vir} \sim 0.7$ Mpc; Drinkwater et al. 2001).

The FDS observations, data quality, and reduction were extensively described in the published FDS papers from Iodice et al. (2016, 2017b, 2019b), Venhola et al. (2017, 2018). In this work we analysed the bright ($m_B \leq 15$ mag) ETGs presented by Iodice et al. (2019b), inside the virial radius of cluster, covered by the inner 9 square degrees around the core. Iodice et al. (2019b) performed the surface photometry of all ETGs in this sample, providing total magnitudes, effective radii, integrated ($g-i$ and $g-r$) colours, and mass-to-light ratios for all galaxies.

2.1. Correction for the PSF

The faint outskirts of galaxies can be contaminated by light scattered from the bright core by the telescope and the atmosphere, which creates artificial haloes. In order to account for this effect, the point spread function (PSF) must be mapped out to a radial distance that is at least comparable to the extent of the galactic halo (Capaccioli & de Vaucouleurs 1983). For VST we derived an extended PSF as described in Appendix B of Capaccioli et al. (2015).

As shown in Capaccioli et al. (2015), the effect of the scattered light is very different at the same surface brightness level between galaxies with large and small angular extent and those which are more or less flattened. In particular, it as been found that the surface brightness profiles of smallest galaxies were marginally affected (∼0.2 mag) by the extended PSF at $\mu_g \sim 29\,\mathrm{mag\,arcsec^{-2}}$, while galaxies with a large angular extent and no bright central nuclei were not significantly affected (∼0.05 mag).

In this work, owing to presence of both small and very elongated galaxies in the studied sample, the amount of scattered light and its effect on the surface brightness profiles needs to be estimated. To this aim, we deconvolved each galaxy in our sample for the VST PSF shown in Capaccioli et al. (2015) via the Lucy-Richardson (hereafter RL) algorithm (Lucy 1974; Richardson 1972).

As expected, the flatter the galaxy, the greater is the effect of the PSF deconvolution on the surface brightness profile. Moreover, smaller round galaxies are also more affected than larger galaxies. The effect of the PSF on the distribution of light from the galaxy is particularly relevant below a surface brightness of 27 mag arcsec^{-2} (r band), but it is however not greater than 0.2 mag for all the analysed galaxies. In Fig. 2 we show an example of the result of the deconvolution on the flattest and the smallest galaxy in our sample.

The effect of the PSF on the surface brightness profiles of the galaxies is illustrated in the rightmost panels of Fig. 2. Beyond 27 mag arcsec^{-2} the deconvolved profiles start to deviate from the original profiles. At radial distances greater than 1 arcmin, the difference between the original and the PSF-corrected profiles is around 0.1 mag arcsec^{-2}.

2.2. Robustness of the deconvolution technique

In order to test the robustness and reliability of our deconvolution technique, we compared the performance of the RL algorithm with the method from Borlaff et al. (2017). These authors estimate the deconvolved image by using the following operations:

$$\mathrm{Residuals} = \mathrm{Image\ raw} - \mathrm{PSF} * \mathrm{Model_{GALFIT}} \quad (1)$$

$$\mathrm{Deconvolved\ Image} = \mathrm{Model_{GALFIT}} + \mathrm{Residuals}, \quad (2)$$

where PSF ∗ Model$_{\mathrm{GALFIT}}$ is the 2D model (with best-fitted parameters) convolved with the adopted PSF, obtained from GALFIT3.0 (Peng et al. 2010), and Model$_{\mathrm{GALFIT}}$ is the 2D model obtained using the best-fit parameters of the galaxy from PSF ∗ Model$_{\mathrm{GALFIT}}$, that is the model of the galaxy without PSF convolution. We applied this technique to galaxies of different sizes. We show the results of this test for one of the smaller galaxies in our sample, FCC 182, since the effect of the deconvolution is much more evident for galaxies with small angular dimensions. The result of this comparison is shown in Fig. 3, from which it is clear that our technique of deconvolution (RL algorithm) is fully consistent with the above method. The same test has also been performed by Raj et al. (2019) for LTGs in FDS, achieving a similar result.

3. Multi-component fit of the light distribution

In the last decade, a big effort was made to model the surface brightness profiles of the brightest cluster and group members to estimate the contribution of the outer envelope to the total light. In this context, there are several observational and theoretical papers in the literature showing that this component appears as an extended, additional exponential-like profile to the azimuthally averaged surface brightness distribution of many ETGs (Seigar et al. 2007; Donzelli et al. 2011; Arnaboldi et al. 2012; Iodice et al. 2016; Spavone et al. 2017, 2018).

Spavone et al. (2017), following the predictions of numerical simulations (Cooper et al. 2013, 2015), described the surface brightness profiles of a sample of ETGs as the superposition of different components: an inner Sérsic profile representing the (sub-dominant) in situ component in the central regions, another Sérsic profile (Sérsic 1963; Caon et al. 1993) representing the (dominant) superposition of the relaxed, phase-mixed accreted components, and an outer diffuse component (the envelope) representing un-relaxed accreted material (streams and other coherent concentrations of debris). The latter component does not contribute any significant surface density to the brighter regions of the galaxy. In order to mitigate the degeneracy between the parameters, Spavone et al. (2017) fixed $n \sim 2$ for the in situ component of their three-component fits, following the predictions of Cooper et al. (2013) for massive galaxies.

As explained in Spavone et al. (2017), since we are interested in the study of the stellar distribution in the outer envelopes of our sample galaxies, we did not use the χ^2 statistics in our fitting procedure. We adopted the same approach described by Seigar et al. (2007) and performed least-squares fits using a Levenberg-Marquardt algorithm, in which the function to be minimised is the root mean square (rms) scatter, defined as $\Delta = \sqrt{\frac{\sum_{i=1}^{m} \delta_i^2}{m}}$, where m is the number of data points and δ_i is the ith residual. In all the fits presented below, the innermost seeing-dominated regions, indicated with dashed lines, were excluded. For further details on the adopted fitting procedure, see Spavone et al. (2017).

Since the ETGs in our sample are in the mass range 8×10^8–$1.2 \times 10^{11}\,M_\odot$, which is partly covered by the available numerical simulations ($10^{10} < M_* \leq 10^{13}\,\mathrm{M_\odot}$), we fitted the surface brightness profiles with multi-component models adopting the fitting technique presented in Spavone et al. (2017), with the only difference that in this work we did not fix the Sérsic index for the first component of the fit, since we have no theoretical predictions about this index for less massive galaxies.

Eleven out of 19 galaxies in the studied sample have masses in the mass range covered by simulations by Cooper et al. (2013). Six of these already have a Sérsic index for the innermost component in the range 1.5–2.5, as predicted by simulations. For

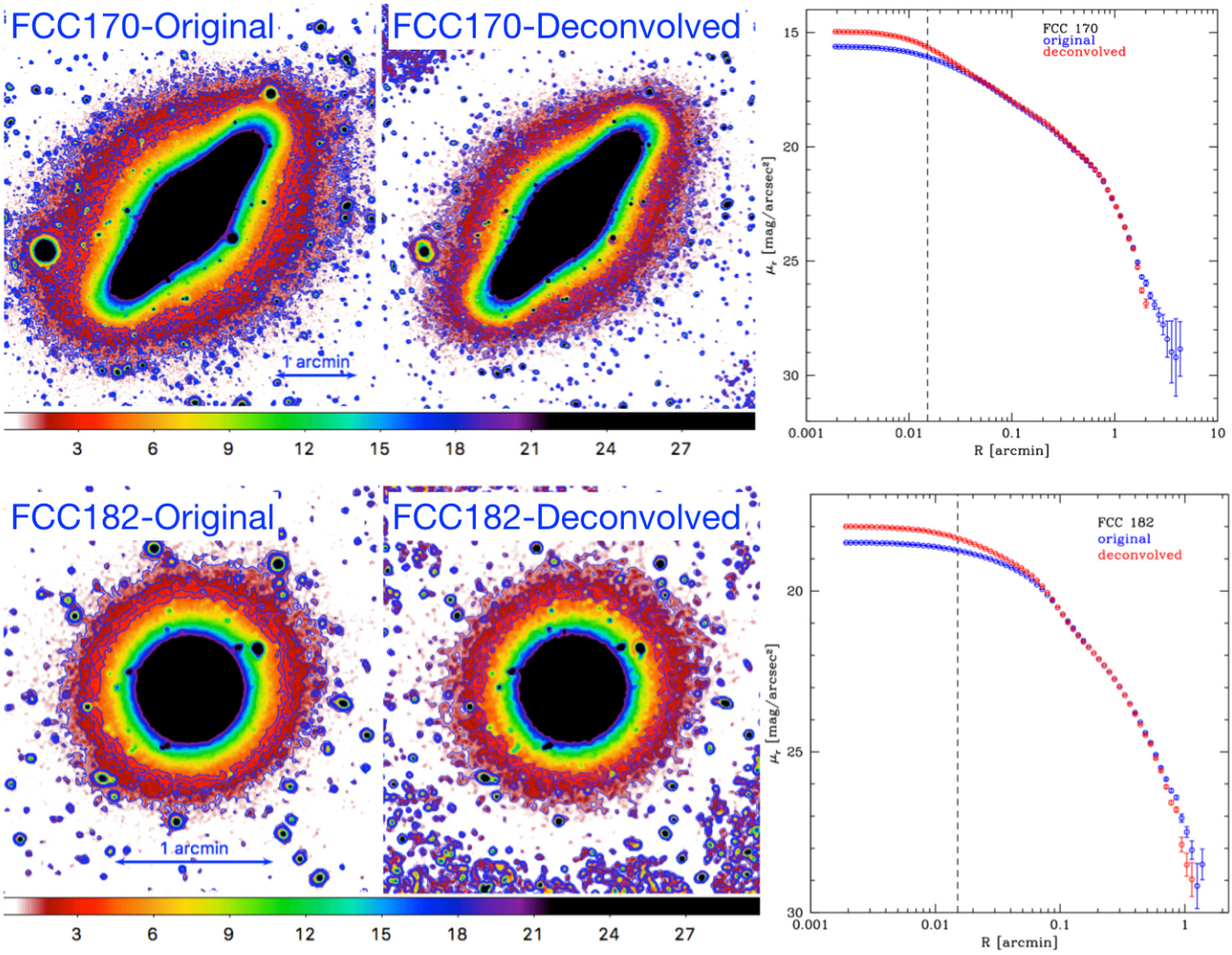

Fig. 2. *Top panel*: original (*left*) and deconvolved (*middle*) images of the flattest galaxy in our sample, FCC170. The original (blue) and deconvolved (red) surface brightness profiles of FCC170 are plotted in the *right panel*. *Bottom panel*: original (*left*) and deconvolved (*middle*) images of the smallest galaxy in our sample, FCC182. The original (blue) and deconvolved (red) surface brightness profiles of FCC182 are plotted in the *right panel*.

the remaining five galaxies we checked how much their accreted mass fractions are affected by fixing $n_1 = 2 \pm 0.5$. We found that the accreted mass fractions range from 1% to 2%, while the rms scatter increases by 5%–20%. Thus, leaving n_1 free reduces the scatter without biasing our results. Results of the fit are shown in Fig. A.1. The best-fitting parameters are reported in Table 1.

Although most of the galaxies analysed in this work are less massive than those studied in simulations, it is worth noticing that the Sérsic index for the in situ component for most of these galaxies falls in the range predicted by Cooper et al. (2013) ($n = 2 \pm 0.5$), as shown in the left panel of Fig. 4. In the right panel of the same figure we plot the distribution of the central surface brightness ($\mu_{0,3}$) of the third component of the fit for galaxies, which are fitted with a third exponential component. For most of these, $\mu_{0,3}$ is fainter than 25 mag arcec^{-2} and the average value of the scale length $r_{h,3}$ is about 165 arcsec. By comparing these values with the typical values obtained for a large sample of disc galaxies from the SDSS data, we found that in the $\mu_0 - r_h$ plane they are all located outside the region in which typical discs are found, with the only exceptions of FCC190 and FCC167 (see Fig. 1 in van der Kruit & Freeman (2011) and references therein). This suggests that these are different components and they are more similar to extended haloes that are found to be exponential.

4. Results: Accreted mass fraction and ICL

Following Spavone et al. (2017), we used the multi-component fits to derive the relative contribution of the accreted component with respect to the total galaxy light, $f_{h,T}$. The accreted mass fraction $f_{h,T}$ is the contribution to the total light of the phase-mixed accreted components plus the envelope (see Sect. 3). The $f_{h,T}$ values are given in Table 1 for all galaxies in the sample, except for FCC153, FCC170, and FCC177. These are the only three edge-on S0 galaxies of our sample. Kinematical studies show that these galaxies possess a bulge and a disc component (see e.g. Pinna et al. 2019a,b; Bedregal et al. 2011; Iodice et al. 2019a). For these objects, in the azimuthally averaged surface brightness profile of the exponential halo would be completely superposed to the exponential disc, and so they would be impossible to disentangle with the photometry alone. For FCC090 the second component of the fit is a Sérsic with $n = 1$, that is an exponential with a central surface brightness of

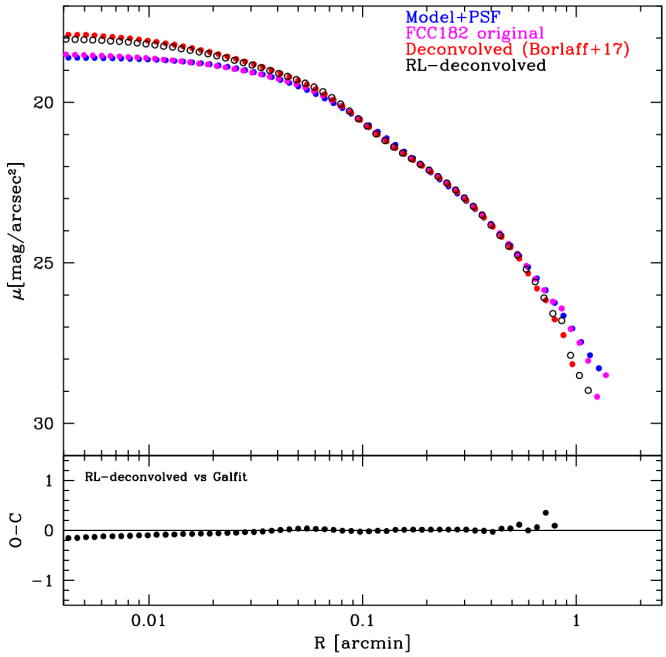

Fig. 3. *Top panel*: deconvolved SB profile using RL algorithm (black) and the method by Borlaff et al. (2017) (red) over-plotted on the original (magenta) and the PSF-convolved model (blue) profiles for FCC 182. *Bottom panel*: residuals between the profile deconvolved with the RL algorithm and that deconvolved with the technique by Borlaff et al. (2017).

22.12 mag arcsec^{-2}, which is typical of discs. This component is reasonably mapping the exponential disc of the galaxy, classified as an S0, and not the accreted material.

For all the other galaxies, we found that the total accreted mass fraction ranges between 27% and 98%. FCC 219 and FCC 213 are the two brightest members in the core centre, and they are so close in projection that their extended stellar envelopes are photometrically indistinguishable. As described in Iodice et al. (2019b), the surface photometry of FCC 219 was derived from the residual image from which the 2D model of FCC 213 is subtracted. Therefore, the stellar envelope that we expect to be present in FCC 219 was partly counted in the extended stellar envelope of FCC 213. As a consequence, according to the stellar mass of FCC 219, the accreted mass fraction we estimate for this galaxy should be considered as a lower limit. Anyway, the less extended stellar envelope in FCC 219 could be consistent with the scenario previously proposed (Forbes et al. 1998; Bekki et al. 2003; Sheardown et al. 2018), where the outer halo of FCC 219 could have been stripped during a past interaction with FCC 213. This is also supported by the low specific frequency of its GCs system, indicating that it has lost many GCs, and thus probably also outer stellar light, into the intra-cluster population around FCC 213. In Fig. 5 we plot the accreted mass fraction $f_{h,T}$ as a function of the projected distance from the cluster centre ($R_{\rm proj}/R_{\rm vir}$; see Table 1 in Iodice et al. 2019a). A clear separation occurs at a cluster-centric distance of about 0.8–1 degree ($R_{\rm proj}/R_{\rm vir} \sim 0.4$–$0.5$): galaxies located inside 1 degree have a higher mass fraction in the outer envelope (≥55%) than those beyond this radius. This distance corresponds to the transition region from the high-to-low-density region of the cluster (where $\Sigma \leq 40$ galaxies Mpc^{-2}), found by Iodice et al. (2019b), at $R \sim 0.4R_{\rm vir}$($\sim$ 0.3 Mpc). As shown by Iodice et al. (2019b), at this radius a decrease in the X-ray emission also occurs.

The majority of the massive ETGs, which are the reddest objects, are located in the high-density region of the cluster (see Fig. 12 in Iodice et al. 2019b), which have higher accreted mass fractions than the galaxies in the low-density regions. The bottom panel of Fig. 5 shows that, on average, the accreted mass fraction also correlates with $(g - i)$ colour. We found that for redder galaxies the contribution of accreted stars to the total mass is higher. Two exceptions are FCC 276 and FCC 083. FCC 276 is the brightest elliptical galaxy on the eastern side of the cluster, at $R_{\rm proj} = 0.4R_{\rm vir}$ from FCC 213 (NGC 1399), in the transition region from high to low density. The location of this galaxy in the cluster reflects its properties. FCC 276 has bluer colours ($g - r \sim 0.3$ mag), comparable colours to the ETGs in the low-density region of the cluster, but a high accreted mass fraction ($f_{h,T} = 0.87$) that is consistent with that typical for all the others ETGs in the high-density region of the cluster, suggesting that this galaxy might be in a transition phase of mass assembly. In particular the bluer colours are related to a distinct kinematical component in the centre ($R \lesssim 10$ arcsec), which has $v_{\rm max} \sim 50$ km s^{-1} and $\sigma \sim 180$ km s^{-1} (Carollo et al. 1997; Iodice et al. 2019b, 2020).

FCC 083 is located on the western side of the cluster at a distance $R_{\rm proj} = 0.85R_{\rm vir}$ from the cluster centre. It is among the brightest and more massive ETGs in the low-density region of the cluster, with very red colours ($g-r \sim 0.67$ mag) and accreted mass fraction comparable with ETGs in the high-density region of the cluster with similar stellar mass (see also Fig. 7).

Fitting the light distribution of all the brightest ETGs inside the virial radius of the Fornax cluster, we can provide a new and more accurate estimate of the ICL in this region of the cluster. The total amount of ICL includes the contributions from the stellar envelope in all galaxies ($R > R_{\rm tr2}$), plus the luminosity of the patch of diffuse light previously detected in the core from Iodice et al. (2017b) and of the stellar bridge connecting NGC 1399 and FCC 184 (Iodice et al. 2016). In the r band, the total luminosity of the ICL is $(2.6 \pm 0.1) \times 10^{11} L_{\odot}$. Taking into account the total magnitude of all the bright galaxies inside the virial radius, from Iodice et al. (2019b) and Raj et al. (2019), as well as that of the dwarf galaxies from Venhola et al. (2017), the total luminosity of the Fornax cluster is $L_{\rm tot} = (7.6 \pm 0.09) \times 10^{11} L_{\odot}$. Therefore, the total fraction of ICL inside the virial radius of the Fornax cluster is $M_{\rm ICL}/M^{*}_{\rm tot} \sim 0.34 \pm 0.20$. Since it is not easy to separate the ICL from the stars that are bound to the BCG, in literature the ratio $(M_{\rm ICL} + M_{\rm BCG})/M^{*}_{\rm tot}$ is also used to measure the ICL fraction (see e.g. Gonzalez et al. 2005). By adopting this approach, for the Fornax cluster we obtain a fraction of $(M_{\rm ICL} + M_{\rm BCG})/M^{*}_{\rm tot} \sim 0.65 \pm 0.30$. In Sect. 6 we compare these values with similar studies for other clusters and with theoretical predictions.

In Fig. 6 we show the average $(g-i)$ colours of ETGs, derived in three galaxy regions: the bright central part inside $0.5R_e$, outside the first transition radius $R > R_{\rm tr1}$, and outside the second transition radius $R > R_{\rm tr2}$ (see Table 1). The bottom panel of this figure shows that, on average, the bright central parts of galaxies in the high-density region of the cluster are redder than those of galaxies in the low-density region, as already shown by Iodice et al. (2019b). Moreover, Iodice et al. (2019a), using the Fornax 3D (F3D) spectroscopic data, found that the central parts of ETGs in the high-density region of Fornax are more metal rich than those in the low-density region, at fixed galaxy mass, suggesting that the difference in colours found from the photometry is due to a difference in metallicity.

The middle panel of Fig. 6 shows the average $(g - i)$ colours derived for $R > R_{\rm tr1}$. The outskirts of the most massive ETGs

Table 1. Best-fitting structural parameters for the 19 bright ETGs inside the virial radius of the Fornax cluster considered in this work.

Object	μ_{e1} [mag arcsec^{-2}]	r_{e1} [arcsec]	n_1	μ_{e2} [mag arcsec^{-2}]	r_{e2} [arcsec]	n_2	$\mu_{0,3}$ [mag arcsec^{-2}]	$r_{h,3}$ [arcsec]	$f_{h,T}$	log M_* [$M_\odot$]	$R_{\rm tr1}$ [kpc]	$R_{\rm tr2}$ [kpc]	$R_{e,r}$ [kpc]	M_r [mag]	$(g-i)$ [mag]
(1)	(2)	(3)	(4)	(5)	(6)	(7)	(8)	(9)	(10)	(11)	(12)	(13)	(14)	(15)	(16)
FCC083	20.85 ± 0.20	20.29 ± 0.24	3.91 ± 0.04	23.73 ± 0.24	71.59 ± 1.97	1.05 ± 0.02	–	–	47% ± 5%	10.30 ± 0.05	5.58	–	3.30	−20.56	1.3
FCC090	20.28 ± 0.80	5.00 ± 0.15	1.64 ± 0.07	23.94 ± 0.17	25.00 ± 0.40	1.00 ± 0.21		–	0	8.91 ± 0.02	1.36	–	1.14	−18.83	0.78
FCC143	18.95 ± 0.05	3.00 ± 0.90	2.03 ± 0.02	21.73 ± 0.02	12.90 ± 0.02	1.33 ± 0.03	26.53 ± 0.07	52.46 ± 0.30	60% ± 9%	9.45 ± 0.01	0.56	6.18	1.03	-18.77	0.97
FCC147	18.88 ± 0.27	5.01 ± 0.75	3.09 ± 0.44	21.44 ± 0.01	33.77 ± 0.70	2.69 ± 0.24	–	–	81% ± 7%	10.38 ± 0.03	0.38	–	2.36	−20.96	0.99
FCC148	19.63 ± 0.55	5.03 ± 0.49	3.11 ± 1.05	20.98 ± 0.61	25.27 ± 2.59	0.96 ± 0.21	24.88 ± 1.11	46.67 ± 14.51	88% ± 9%	9.76 ± 0.04	0.47	11	2.73	-19.79	0.86
FCC153	19.11 ± 0.61	15.28 ± 4.11	1.04 ± 0.14	22.23 ± 0.11	40.68 ± 3.68	0.50 ± 0.40	–	–	–	9.88 ± 0.01	4.29	-	2.00	-19.89	0.77
FCC161	19.66 ± 0.54	5.00 ± 0.29	5.00 ± 0.31	20.84 ± 0.58	26.65 ± 3.94	1.58 ± 0.55	25.29 ± 0.71	109.37 ± 18.91	91% ± 8%	10.42 ± 0.03	0.27	13.89	2.76	-21.02	1.04
FCC167	19.83 ± 0.41	23.94 ± 5.04	2.70 ± 0.68	21.43 ± 0.74	56.86 ± 8.32	0.40 ± 0.96	21.43 ± 0.81	44.55 ± 14.72	63% ± 7%	10.99 ± 0.05	4.32	12.33	5.80	-22.36	1.03
FCC170	18.58 ± 0.53	6.22 ± 1.94	2.73 ± 1.19	20.36 ± 0.82	27.63 ± 3.23	0.93 ± 0.35	–	–	–	10.35 ± 0.02	0.86	–	1.69	−20.71	1.07
FCC177	19.06 ± 0.19	2.00 ± 0.26	1.35 ± 0.45	20.63 ± 0.02	27.04 ± 0.12	0.86 ± 0.08	–	–	–	9.93 ± 0.02	0.21	–	3.48	−19.71	1.08
FCC182	19.77 ± 0.16	3.00 ± 0.62	0.92 ± 0.10	22.21 ± 0.22	12.54 ± 0.66	1.25 ± 0.14	–	–	65% ± 5%	9.18 ± 0.02	0.47	–	0.94	−17.88	1.03
FCC184	18.05 ± 0.57	5.19 ± 0.58	1.91 ± 0.39	21.27 ± 0.34	37.02 ± 7.18	1.53 ± 0.90	25.98 ± 0.26	229.09 ± 3.23	75% ± 11%	10.67 ± 0.01	0.93	17.40	3.22	-21.43	1.14
FCC190	20.07 ± 0.02	4.02 ± 1.50	1.44 ± 0.04	21.12 ± 0.03	13.10 ± 0.23	0.54 ± 0.01	21.32 ± 0.02	18.32 ± 0.10	85% ± 7%	9.73 ± 0.03	0.47	2.36	1.80	-19.28	1.04
FCC193	18.96 ± 0.32	9.12 ± 1.87	2.27 ± 0.27	22.80 ± 0.75	54.36 ± 9.61	1.28 ± 0.62	26.59 ± 0.83	387.26 ± 33.98	60% ± 6%	10.52 ± 0.04	2.82	20.35	2.90	-20.93	1.17
FCC219	18.46 ± 0.03	12.48 ± 1.66	2.13 ± 0.02	24.54 ± 0.02	291.58 ± 1.94	3.23 ± 0.04	–	–	67% ± 14%	11.10 ± 0.01	3.79	–	15.77	−22.95	0.96
FCC276	17.55 ± 0.25	3.00 ± 0.29	1.85 ± 0.24	20.87 ± 0.23	32.81 ± 1.10	1.75 ± 0.26	23.68 ± 0.31	99.45 ± 2.02	87% ± 4%	10.26 ± 0.03	0.46	12.54	4.24	-21.31	0.64
FCC277	20.14 ± 0.15	7.64 ± 0.32	1.66 ± 0.13	21.88 ± 0.16	20.88 ± 0.23	1.38 ± 0.17	–	–	60% ± 8%	9.53 ± 0.01	1.04	–	1.28	−19.24	0.77
FCC301	19.15 ± 0.10	5.85 ± 0.11	1.30 ± 0.07	23.56 ± 0.11	26.53 ± 2.15	0.60 ± 0.07	–	–	26% ± 1%	9.30 ± 0.05	1.80	–	1.12	−18.82	0.70
FCC310	21.12 ± 0.23	18.62 ± 2.26	1.62 ± 0.22	25.71 ± 0.93	61.41 ± 5.15	0.20 ± 0.3	–	–	14% ± 6%	9.73 ± 0.02	7.99	–	3.43	−19.70	0.77

Notes. Columns 2, 3, and 4 report the effective surface brightness and effective radius for the inner component of each fit. Columns 5, 6, 7 list the same parameters for the second component, whereas Cols. 8 and 9 list the central surface brightness and scale length for the outer exponential component. Column 10 gives the accreted mass fraction derived from our fit. Column 11 reports the total stellar mass, while Cols. 12 and 13 report the transition radii derived by the intersection between the first and the second component of the fit and the second and the third component, respectively. Columns 14, 15, and 16 give the effective radii, absolute magnitudes in the r band, and average $(g-i)$ colours from Iodice et al. (2019b)

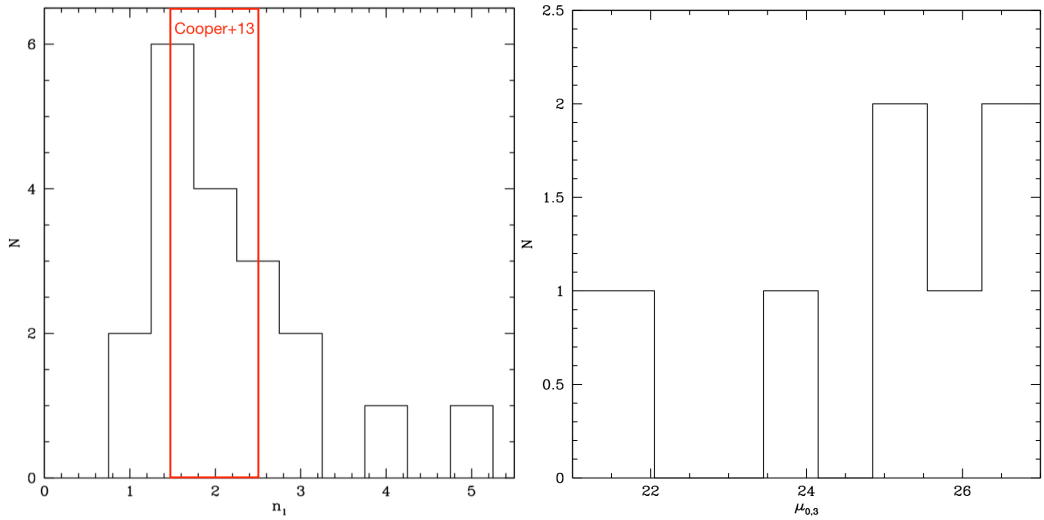

Fig. 4. *Left panel*: distribution of the Sérsic index of the innermost component of our fit for the 19 analysed galaxies. The red region brackets the range of n_1 in the simulations by Cooper et al. (2013). *Right panel*: distribution of the central surface brightness of the 8 galaxies in the sample having a third exponential component ($\mu_{0,3}$).

($M \geq 10^{10}\,M_\odot$) in the high-density region are bluer than the central parts, as can be clearly seen by comparing the least-squares fit of the values inside $0.5R_e$ with that for $R > R_{\rm tr1}$. Taking errors into account, there is no appreciable difference in colour between inner parts and outskirts for the ETGs in the low-density regions.

As presented in Sect. 3, for the most massive ETGs ($M \geq 10^{10}\,M_\odot$) in our sample, by fitting the surface brightness profile, we identified a third outer component that dominates the light beyond a second transition radius (see Table 1). All these galaxies are located in the high-density region of the cluster and, by comparing the average colours in their centres ($R < 0.5R_e$) and for $R > R_{\rm tr1}$, it seems that the colour distribution remains very constant (see top panel of Fig. 6). The same conclusion can be drawn by looking at the average $(g-i)$ colour profiles shown in Fig. 7. These are derived in three different bins of stellar mass: low-mass galaxies with $8.9 \leq \log M_*/M_\odot \leq 10.5$, intermediate-mass galaxies with $10.5 \leq \log M_*/M_\odot \leq 10.8$, and high-mass galaxies with $10.8 \leq \log M_*/M_\odot \leq 11.2$.

In Fig. 7, the average values of $R_{\rm tr1}$ and $R_{\rm tr2}$ are plotted as dashed and continuous arrows, respectively, on each colour profile. At each transition radius corresponds to a change in the colour trend. For the intermediate and massive galaxies, colours in the outer regions (i.e. for $R \geq R_{\rm tr1}$) are bluer than those in the central regions, and for $R > R_{\rm tr1}$ and $R > R_{\rm tr2}$ the colour profiles tend to flatten, thereby confirming the lack of a significant colour gradient. All galaxies in these two mass bins are located in the high-density region of the cluster. It is also worth noting that the galaxies in these two mass bins show a clear increase towards redder colours ($g-i \sim 1.1$–1.3 mag), in the centre, for $R \leq R_{\rm tr1}$.

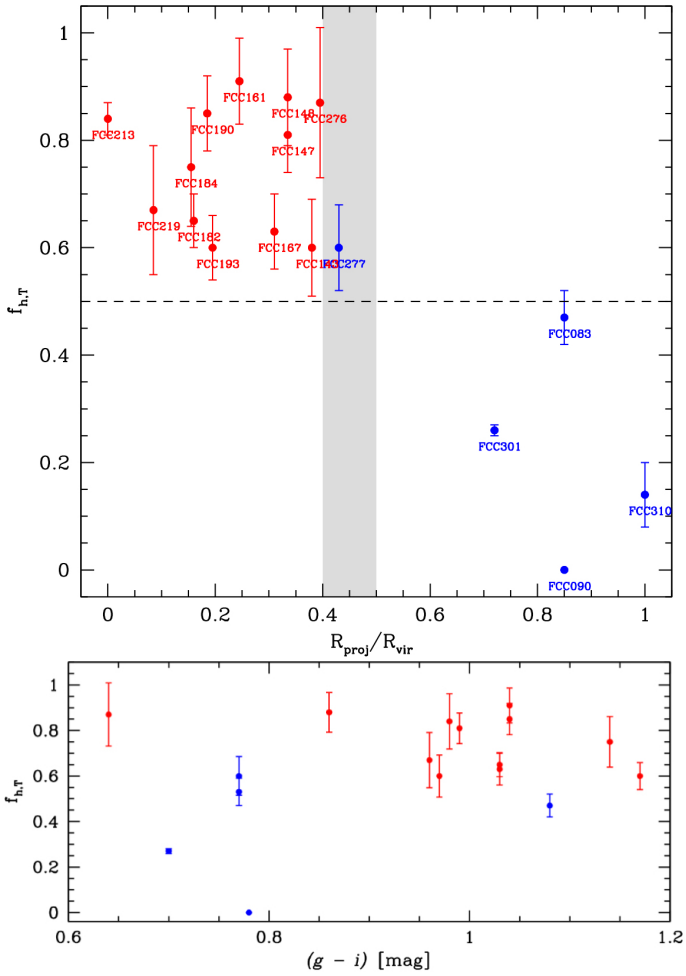

Fig. 5. *Top panel*: accreted mass fraction as a function the projected distance from the cluster centre, normalised to the virial radius of the cluster (R_{vir} = 0.7 Mpc, Drinkwater et al. 2001). Red dots indicate galaxies in the high-density region of the cluster, while blue dots indicate galaxies in the low-density region. The vertical grey region shows the range of cluster-centric distance where a clear separation occurs: galaxies located inside ∼0.8–1 degree from the core of the cluster show a higher outer envelope mass fraction. *Bottom panel:* accreted mass fraction as a function of the $(g - i)$ average colour for galaxies in the low- (blues dots) and high- (red dots) density regions of the cluster. On average, redder galaxies have higher accreted mass fractions. FCC 277 is in the transition region from high-to-low density; this region has a higher accreted mass fraction, but has colours comparable with galaxies in the low-density region.

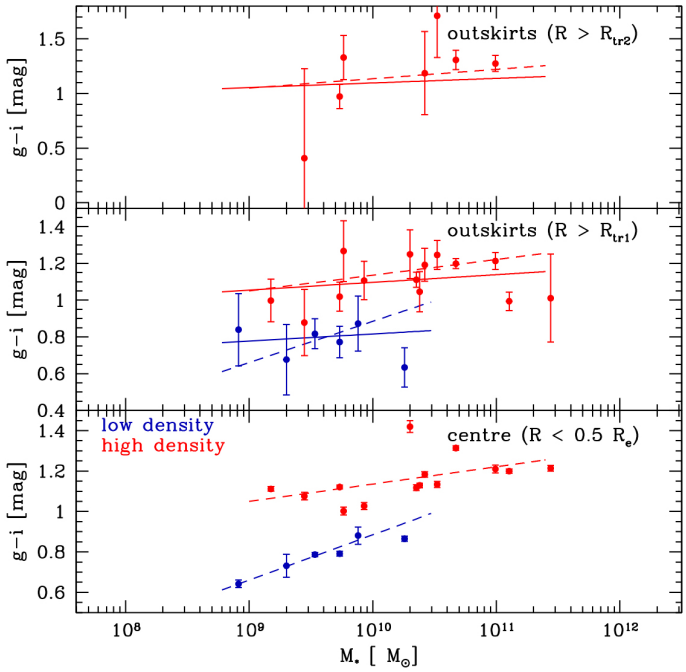

Fig. 6. Average colours $(g - i)$ for the central parts ($R < 0.5R_e$, *bottom panel*), for $R > R_{tr1}$ (middle panel), and for $R > R_{tr2}$ (*top panel*) of the FDS ETGs located in the high- (red circles) and low-density region (blue circles) of the cluster as a function of the total stellar mass. The red and blue dashed lines in all the panels represent the least-square fits of the values for the central parts ($R < 0.5R_e$) of the ETGs in the high- and low-density regions of the cluster, respectively. The continuous red and blue lines in the *middle panel* are the least-square fits of the values for $R > R_{tr1}$, while the dashed and the continuous red lines in the *top panel* are the least-square fits of the values for $R < 0.5R_e$ and $R > R_{tr1}$, respectively.

The low-mass ETGs, both in the high- and low-density region of the cluster, exhibit bluer colours in the central regions ($R \leq R_{tr1}$), as already pointed out by Iodice et al. (2019b).

5. Observations versus simulations

The main aim of this section is to provide a direct comparison between the observables we derived from the surface photometry (i.e. light and colour distribution) of the ETGs inside the virial radius of the Fornax cluster and the theoretical predictions for the same quantities.

5.1. Shape of the light profiles

According to Cooper et al. (2015), the surface brightness profile of an ETG should be described well by the superposition of (i) an inner Sérsic profile, where $n \sim 2$, representing the (sub-dominant) in situ component in the central regions; (ii) a second Sérsic profile, describing the (dominant) "relaxed" accreted component; (iii) and an outer diffuse envelope, comprised of the "un-relaxed" accreted material. This un-relaxed component, which has an exponential decline and a central surface brightness $\mu_0 \sim 26$ mag arcsec^{-2} in the r band, dominates the light distribution at smaller transition radius for the most massive galaxies ($\geq 10^{12} M_\odot$). The stellar population of the in situ component is expected to be very similar to the dominant relaxed accreted component. As they are well mixed together, the sum of these two components is expected to have a smooth distribution with only faint features to suggest they are distinct. The outer envelope is comprised of streams and other coherent concentrations of debris, tracing the latest phase of the mass assembly. This component contributes only for a small fraction (≤20%) to the total accreted mass.

The fits of the surface brightness profiles presented in Sect. 3 are largely consistent with the theoretical predictions summarised above. In particular, we found that the dominant component to the light distribution is the relaxed accreted, which is reproduced well by the second Sérsic law. In the majority of ETGs, the in situ component, which is also fitted with a Sérsic law, has $n \simeq 1$–3, with a distribution peak at $n \sim 2$ (see Fig. 4). The outer envelope in all galaxies that show this component is closely fitted by an exponential law, with an average central surface brightness of $\mu_{0,3} \sim 25$ mag arcsec^{-2} and scale radius of $r_{h,3} \sim 165$ arcsec (∼16 kpc, see Table 1).

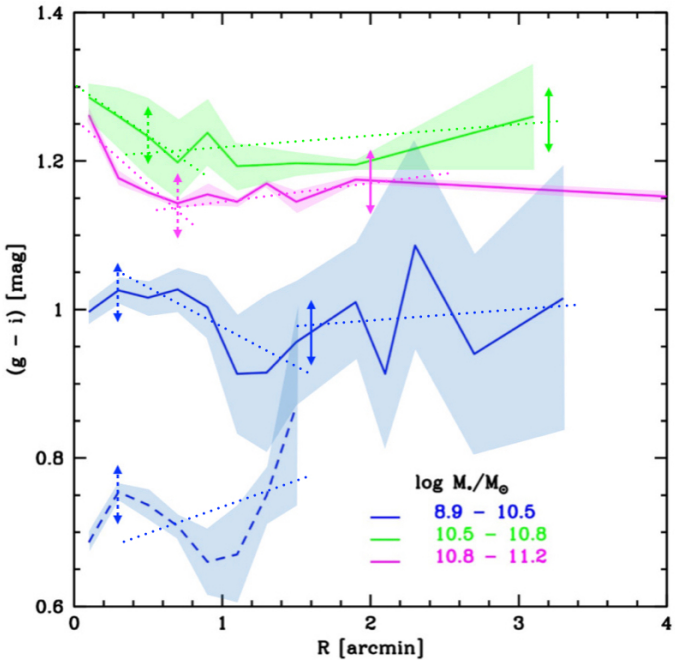

Fig. 7. Running mean of the average $(g - i)$ colour profiles of the ETGs in Fornax, in three different mass bins: $8.9 \leq \log M_*/M_\odot \leq 10.5$ (blue), $10.5 \leq \log M_*/M_\odot \leq 10.8$ (green), and $10.8 \leq \log M_*/M_\odot \leq 11.2$ (magenta). Blue dashed line indicates galaxies in the low-density region, while the blue continuous line indicates those in the high-density region of the cluster. The dashed and the continuous vertical arrows denote the position of the average transition radii, $R_{\rm tr1}$ and $R_{\rm tr2}$ respectively, in each mass bin. The dotted lines represent the fits to the colour gradients between transition radii.

Therefore, this component has a comparable central surface brightness, but a smaller scale radius, to those found in similar observational studies that are mainly based on BCGs, where the outer envelope has $24 \leq \mu_0 \leq 26$ mag arcsec^{-2} and $30 \leq r_h \leq 100$ kpc, in the r band (Seigar et al. 2007; Donzelli et al. 2011; Spavone et al. 2017). The less extended envelope (i.e. smaller $r_{h,3}$) in the ETGs in Fornax is expected since they are less massive galaxies than the BCGs studied in the works cited above (see also Sect. 5.2).

5.2. Accreted mass fraction versus total stellar mass

In Fig. 8 (left panel) we compare the accreted mass ratios derived for the most massive FDS galaxies ($1.8 \times 10^{10}\, M_\odot \leq M_\star \leq 12.7 \times 10^{10}\, M_\odot$) with the theoretical predictions from semi-analytic, particle-tagging simulations by Cooper et al. (2013, 2015) and the Illustris TNG cosmological hydrodynamical simulations by Pillepich et al. (2018).

Figure 8 also includes previous estimates of the total accreted mass fraction for BCGs from the literature based on deep images and the same fitting technique (Seigar et al. 2007; Bender et al. 2015; Iodice et al. 2016, 2017b, 2020; Spavone et al. 2017, 2018; Cattapan et al. 2019). Since we are comparing the accreted mass fraction derived both for bright cluster members and for the brightest galaxies at the centre of less dense environments as in the group of galaxies, from this comparison there is a clear indication that the driving factor for the accreted mass is the total stellar mass of the galaxy, independent from the environment. This is in agreement with theoretical predictions, which are included in Fig. 8. In the Fornax cluster, for massive galaxies ($\geq 10^{10}\, M_\odot$) the stars accreted account for most of the total galaxy stellar mass. A good agreement is also found in the lower-mass regime ($\leq 10^{10}\, M_\odot$), which remains still quite poorly explored on both theoretical and observational sides. In the right panel of Fig. 8, we compare the estimate of the accreted mass fraction for the less massive galaxies in the Fornax cluster (FCC090, FCC301, and FCC310) with predictions from Tacchella et al. (2019) for Illustris TNG galaxies in the mass range 10^9–$10^{11.5}\, M_\odot$. We find that in this range of stellar masses the accreted fraction is quite low ($f_{h,T} \leq 26\%$), as also predicted by simulations.

5.3. Colour gradients in the stellar haloes

The three bins of stellar masses given in Sect. 5.3 and in Fig. 7 were chosen to allow a direct comparison with the predictions based on Illustris TNG simulations by Tacchella et al. (2019). These authors found that, at fixed M_*, galaxies with higher spheroid-to-total ratio (S/T) have an higher fraction of accreted mass, and that this morphological indicator is strongly correlated with galaxies stellar mass. They also found that the S/T ratio varies with the average $(g - r)$ colour, wherein redder galaxies have higher S/T ratios, and that this is especially true for $M_* \simeq 10^{10.5}$–$10^{11}\, M_\odot$. Compared to the Fornax cluster, this mass range includes all ETGs in the high-density region of the cluster, which are the redder objects of the sample and where the higher accreted mass fraction is found; this is consistent with the theoretical predictions cited above. As expected, the most massive galaxies exhibit a colour gradient (La Barbera et al. 2012), from the central regions to the first transition radius ($R_{\rm tr1}$), while beyond this radius, the average colour profile tends to flatten. For the less massive galaxies instead, this flattening is observed in the outskirts, beyond $\sim R_{\rm tr2}$. A similar behaviour is also predicted for the metallicity in simulations by Cook et al. (2016). This flattening is due to the ongoing accretion of stars coming from different satellite galaxies, which produces a mixing of different stellar populations. The link between the transition radii and the variations in the colour trend allows us to establish a correlation between the different components identified in the surface brightness profiles and their colours, that is their stellar populations.

5.4. Intracluster light

In this work we have provided the first accurate estimate of the ICL fraction inside the virial radius of the Fornax cluster, which amounts to about 34% (see Sect. 4). Using deep imaging, Mihos et al. (2017) estimate an ICL fraction for the Virgo cluster ranging between 7% and 15%. For the Coma cluster, there are several studies that quote the ICL, ranging from 25% up to 50% (Melnick et al. 1977; Thuan & Kormendy 1977; Bernstein et al. 1995; Adami et al. 2005; Jiménez-Teja et al. 2019). Moreover, in a compilation of ICL estimates for nearby clusters, Ciardullo et al. (2004) found that the ICL fraction spans the range of 15%–35%. Gonzalez et al. (2005) adopted a different approach in the study of 23 nearby galaxy clusters and groups, spanning a halo mass from 10^{13} to $10^{15}\, M_\odot$. They provided the fraction of ICL with respect to the luminosity of BCG+ICL and they found that ICL/BCG+ICL ratio is ~50% for clusters of galaxies with a halo mass comparable to that of the Fornax cluster, i.e. $\sim 10^{14}\, M_\odot$. For the Fornax cluster we derive ICL/BCG+ICL ~65%.

Theoretical simulations tailored to studying the ICL component in clusters (Rudick et al. 2011; Contini et al. 2014) found

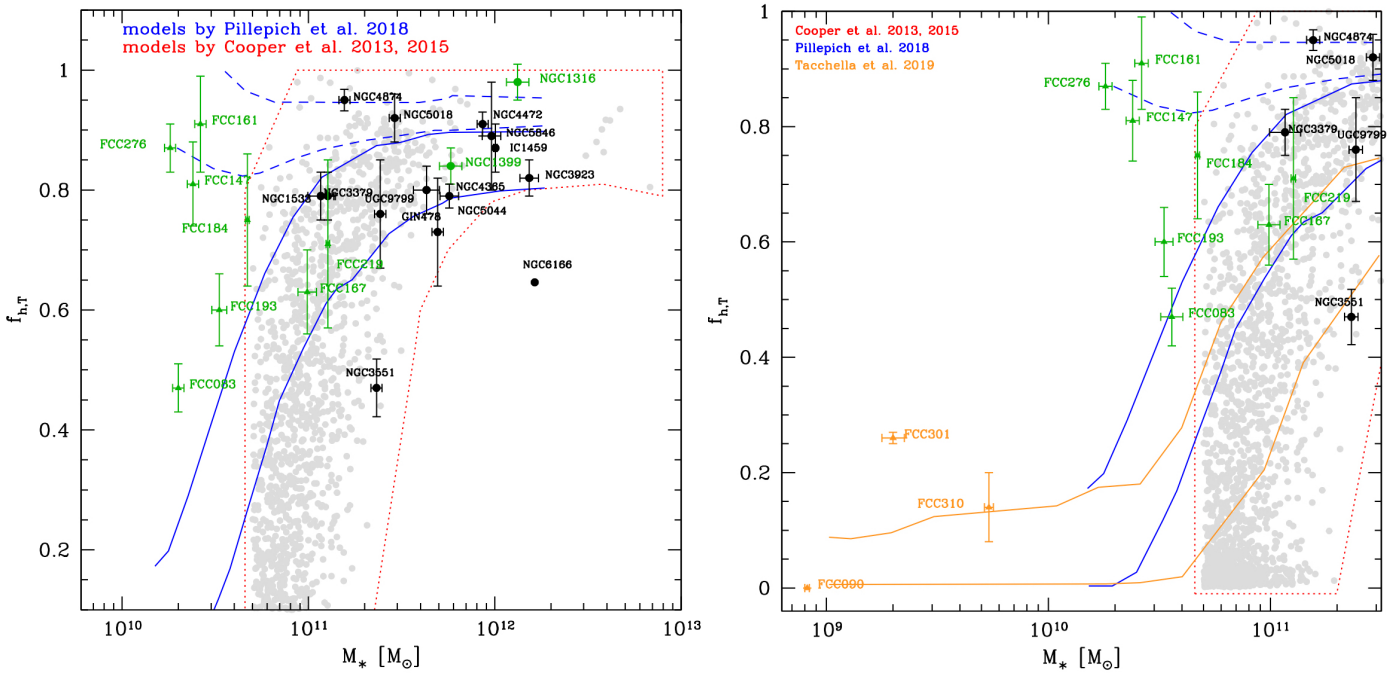

Fig. 8. *Left panel:* accreted mass fraction vs. total stellar mass for ETGs. The measurements for FDS galaxies analysed in this work are given as green triangles. The green circles correspond to the FDS galaxies NGC1399 and NGC1316, published by Iodice et al. (2016, 2017b). The black circles correspond to other BCGs from the literature (Seigar et al. 2007; Bender et al. 2015; Spavone et al. 2017, 2018; Iodice et al. 2020; Cattapan et al. 2019). The red region, enclosing grey dots, indicates the predictions of cosmological galaxy formation simulations by Cooper et al. (2013, 2015). The blue continuous and dashed regions indicate the accreted mass fraction measured within 30 kpc and outside 100 kpc, respectively, in Illustris simulations by Pillepich et al. 2018 (see their Fig. 12). *Right panel:* same as the left panel for less massive galaxies in the FDS sample (orange triangles). Orange regions indicate the accreted mass fraction for low-mass galaxies in Illustris TNG simulations by Tacchella et al. (2019).

that this accounts for ∼10%−40% of the total light of the cluster, with no dependence from the halo mass. In Fig. 9 we compare the ICL estimate derived for the Fornax cluster, as well as the available estimates for Coma and Virgo clusters, with theoretical predictions provided by Contini et al. (2014). These authors measured the ICL fraction considering all galaxies inside the virial radius of the cluster and with stellar masses larger than $10^8\ M_\odot$; thus, their values are consistent with the range of stellar masses for galaxies inside the virial radius of the Fornax cluster. Despite the differing techniques used to estimate the total ICL fraction, these values are reasonably in agreement with predicted values.

As suggested by theoretical works cited above, the amount of ICL is an indicator of the evolutionary stage of a cluster, with more evolved clusters having a higher ICL fraction. This would account for the different estimates derived for the Fornax cluster with respect to the Virgo and Coma clusters. The higher ICL fraction found in Fornax is consistent with an evolved state, since most of the bright (m_B < 15 mag) cluster members have transformed into ETGs (with an ETGs/LTGs ratio of 1.6 inside the virial radius) more than in the Virgo cluster, where the ETGs/LTGs ∼0.62 (Ferguson 1989).

The Coma cluster appears in a more evolved phase with respect to the Fornax cluster, since the majority of the 200 most luminous galaxies are ellipticals and S0s, with ETGs/LTGs ratio of 6 (Colless et al. 2000), and has a comparable ICL fraction to that in the Fornax cluster. On the other hand, the low ETGs/LTGs ratio of the Virgo cluster could consistently indicate an earlier evolutionary phase and therefore an expected lower fraction of ICL, as shown in Fig. 9.

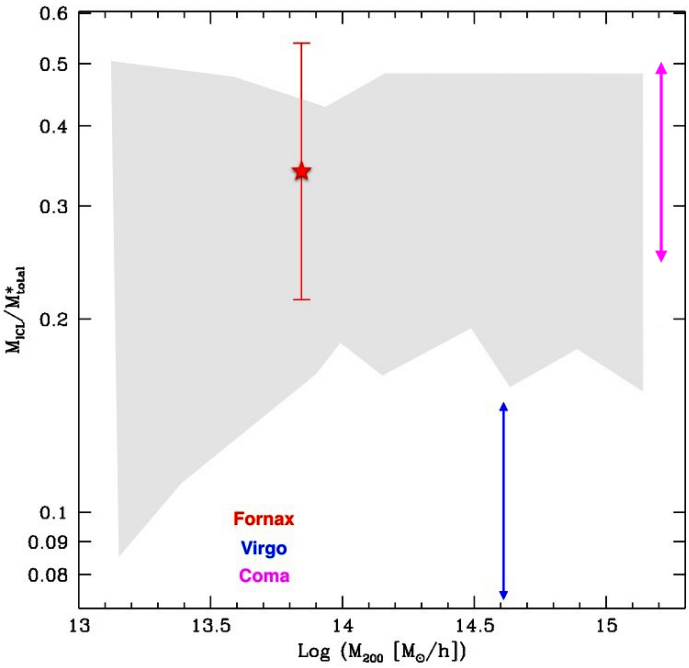

Fig. 9. Fraction of ICL as a function of halo mass for Fornax (red star). The ranges of ICL fractions for Virgo (Mihos et al. 2017) and Coma (Melnick et al. 1977; Thuan & Kormendy 1977; Bernstein et al. 1995; Adami et al. 2005; Jiménez-Teja et al. 2019) are given as blue and magenta arrows, respectively. The grey shaded region encloses all the median results from different models by Contini et al. (2014; see their Fig. 2). For the Fornax cluster, as well as for Virgo and Coma cluster, M_{200} is the virial mass.

6. Discussion: Accreted mass fraction versus cluster-centric distance

In this work we have studied the light and colour distribution of the brightest ETGs inside the virial radius of the Fornax cluster, using deep, multi-band images from the FDS with VST (Iodice et al. 2019b; Venhola et al. 2018). The large integration time and wide covered area of FDS data allow us to map the light and colour distributions down to $\mu_g \geq 27$ mag arcsec^{-2}, therefore out to the regions of stellar haloes and ICL regime. The main aim of the present work is to estimate the total accreted mass fraction in each galaxy of the sample and correlate this fraction with the assembly history of the Fornax cluster that emerged from previous studies. In addition, having a complete coverage of the Fornax cluster out to its virial radius down to such a LSB regime, we are also able to provide an accurate estimate of the ICL inside this region of the cluster.

Our main results can be summarised as follows:

– The highest accreted mass fraction (50%–90%) is found in the massive ($10^{10} \leq M \leq 10^{12}\,M_{\odot}$) and reddest ETGs located in the high-density region of the cluster ($\leq 0.4 R_{\rm vir} \sim 0.3$ Mpc). For all ETGs in the low-density region, even for those with comparably high stellar masses as ETGs in the high-density region, we found a lower accreted mass fraction (less than 50%).
– The accreted mass fractions derived for the ETGs in Fornax are consistent with those from theoretical predictions and with previous observational estimates.
– The colour profiles of the ETGs with the largest accreted mass fraction, on average, tend to flatten in the outskirts of the galaxy, that is beyond the transition radius from the central in situ component to the ex situ accreted component.
– The total luminosity of the ICL compared with the total luminosity of all cluster members (bright galaxies and dwarfs), inside the virial radius of the cluster, is about 34%.

The new findings closely fit the complex picture emerging for the assembly history of the Fornax cluster in the latest years. By combining the structural properties of the galaxies from the FDS data and high-resolution MUSE data from F3D (i.e. morphology, colours, kinematics, and stellar population), we know that the cluster shows three well-defined groups of galaxies: the core, the NS clump and the infalling galaxies (see Fig. 1). Galaxies in each group have different properties in their light and colour distributions, kinematics, and stellar populations (Iodice et al. 2019a). In particular, the clump galaxies are in the highest range of stellar masses; they are the reddest and more metal-rich galaxies of the sample. Their outskirts have lower metallicity than the bright central regions, which is an indication that the mass assembly of metal-poor satellites proceeded in the outskirts.

The infalling galaxies are distributed nearly symmetrically around the core, in the low-density region of the cluster. The majority are LTGs with ongoing star formation and show signs of interaction with the environment and/or minor merging events in the form of tidal tails and disturbed molecular gas (Zabel et al. 2019; Raj et al. 2019). The ETGs belonging to this group are less massive and bluer than the ETGs in the clump. In this region, galaxies have on average lower metallicities with respect to galaxies in the clump.

The ETGs showing the largest accreted mass fraction and flat colour profiles in the outskirts are all the galaxies populating the clump. The few ETGs with a small amount of accreted mass, in the low-density region of the cluster, belong to the infalling galaxies (see also Fig. 1).

As suggested by Iodice et al. (2019a), the clump may result from the early accretion of a group of galaxies during the gradual build-up of the cluster, which induced the observed asymmetry in the spatial distribution of the brightest galaxies. Because of the lower velocity dispersion in galaxy groups, the cluster members accreted as part of groups can undergo pre-processing and gravitational interactions that modified their structure and favoured the growth of the stellar haloes. This would explain the high fraction of kinematically decoupled components in the galaxies belonging to the clump, the thick discs observed in the three edge-on S0 galaxies (Pinna et al. 2019b,a), and, as result of the present work, also the large fraction of accreted mass in the galaxies in this group. Consistent with this picture, a previous analysis of the FDS data showed that the region of the cluster where the clump is located is the only region inside the virial radius where intra-cluster baryons were found (Iodice et al. 2016, 2019b; Spiniello et al. 2018). Therefore, also taking into account that the ETGs in the clump have the largest accreted mass fraction, we can conclude that the major contribution to the total ICL inside the virial radius of the cluster comes from this region.

The observed properties of the infalling galaxies (late-type structures, bluer colours, active star formation, low metallicity, and disturbed morphology) suggest that they can be considered as galaxies that are entering the cluster. The ETGs belonging to this group are locally isolated systems (FCC 083, FCC 090, FCC 301, and FCC 310 in Fig. 1) in the low-density region of the cluster. Compared to the galaxies in the clump, they do not yet undergo many galaxy-galaxy interactions or merging that might have triggered the mass assembly process and, as a consequence, they show the lowest fraction of accreted mass.

In conclusion, the main results of this work strongly suggest that, inside the Fornax cluster, there is a clear indication that the driving factor for the accretion process is the total stellar mass of the galaxy. These results agree with the hierarchical accretion scenario, which also shapes the environment where the galaxies reside. The galaxies with the highest accreted mass are in fact located in the high-density region of the cluster. In this framework, the galaxies in the clump went through the mass accretion in small groups where they resided before merging into the cluster potential (see e.g. Raj et al. 2020, for the Fornax-A group). Therefore, at the present epoch of the Fornax assembly history, they are shaping the high-density region of the cluster, which is the major contribution to the stellar density in the core of the cluster.

Acknowledgements. The authors are very grateful to the anonymous referee for his/her comments and suggestions which helped to improve and clarify the paper. This work is based on visitor mode observations taken at the ESO La Silla Paranal Observatory within the VST Guaranteed Time Observations, Programme IDs 094.B-0512(B), 094.B- 0496(A), 096.B-0501(B), 096.B-0582(A). MS and EI acknowledge financial support from the VST project (P. I. P. Schipani), and wish to thank P. T. de Zeeuw, O. Gerhard, A. Pillepich, R. S. Remus and D. A. Forbes for useful discussions and suggestions. Authors wish to thank ESO for the financial contribution given for the visitor mode runs at the ESO La Silla Paranal Observatory. EI, MAR, RP, NRN and AV acknowledge financial support from the European Union Horizon 2020 research and innovation programme under the Marie Skodowska-Curie grant agreement n. 721463 to the SUNDIAL ITN network. NRN acknowledges financial support from the "One hundred top talent program of Sun Yat-sen University" Grant N. 71000-18841229. GvdV acknowledges funding from the European Research Council (ERC) under the European Union's Horizon 2020 research and innovation programme under grant agreement No 724857 (Consolidator Grant ArcheoDyn). J.F-B acknowledges support through the RAVET project by the grant AYA2016-77237-C3-1-P from the Spanish Ministry of Science, Innovation and Universities (MCIU) and through the IAC project TRACES which is partially supported through the state budget

and the regional budget of the Consejería de Economía, Industria, Comercio y Conocimiento of the Canary Islands Autonomous Community. AV thanks the Eemil Aaltonen foundation for the financial support. GvdV acknowledges funding from the European Research Council (ERC) under the European Union's Horizon 2020 research and innovation programme under grant agreement No 724857 (Consolidator Grant ArcheoDyn). We thank the organisers of the "Light in the suburbs" conference for the many stimulating discussions during the conference.

References

Adami, C., Slezak, E., Durret, F., et al. 2005, A&A, 429, 39
Amorisco, N. C. 2017, MNRAS, 469, L48
Arnaboldi, M., Ventimiglia, G., Iodice, E., Gerhard, O., & Coccato, L. 2012, A&A, 545, A37
Barbosa, C. E., Arnaboldi, M., Coccato, L., et al. 2018, A&A, 609, A78
Bedregal, A. G., Cardiel, N., Aragón-Salamanca, A., & Merrifield, M. R. 2011, MNRAS, 415, 2063
Bekki, K., Forbes, D. A., Beasley, M. A., & Couch, W. J. 2003, MNRAS, 344, 1334
Bender, R., Kormendy, J., Cornell, M. E., & Fisher, D. B. 2015, ApJ, 807, 56
Bernstein, G. M., Nichol, R. C., Tyson, J. A., Ulmer, M. P., & Wittman, D. 1995, AJ, 110, 1507
Borlaff, A., Eliche-Moral, M. C., Beckman, J. E., et al. 2017, A&A, 604, A119
Cantiello, M., D'Abrusco, R., Spavone, M., et al. 2018, A&A, 611, A93
Caon, N., Capaccioli, M., & D'Onofrio, M. 1993, MNRAS, 265, 1013
Capaccioli, M., & de Vaucouleurs, G. 1983, ApJS, 52, 465
Capaccioli, M., Spavone, M., Grado, A., et al. 2015, A&A, 581, A10
Carollo, C. M., Franx, M., Illingworth, G. D., & Forbes, D. A. 1997, ApJ, 481, 710
Cattapan, A., Spavone, M., Iodice, E., et al. 2019, ApJ, 874, 130
Ciardullo, R., Mihos, J. C., Feldmeier, J. J., Durrell, P. R., & Sigurdsson, S. 2004, in Recycling Intergalactic and Interstellar Matter, eds. P. A. Duc, J. Braine, & E. Brinks, IAU Symp., 217, 88
Coccato, L., Gerhard, O., Arnaboldi, M., et al. 2010, Highlights Astron., 15, 68
Coccato, L., Gerhard, O., Arnaboldi, M., & Ventimiglia, G. 2011, A&A, 533, A138
Coccato, L., Arnaboldi, M., & Gerhard, O. 2013, MNRAS, 436, 1322
Colless, M. 2000, in Coma Cluster, ed. P. Murdin, 2600
Contini, E., De Lucia, G., Villalobos, Á., & Borgani, S. 2014, MNRAS, 437, 3787
Contini, E., Yi, S. K., & Kang, X. 2019, ApJ, 871, 24
Cook, B. A., Conroy, C., Pillepich, A., Rodriguez-Gomez, V., & Hernquist, L. 2016, ApJ, 833, 158
Cooper, A. P., Cole, S., Frenk, C. S., et al. 2010, MNRAS, 406, 744
Cooper, A. P., D'Souza, R., Kauffmann, G., et al. 2013, MNRAS, 434, 3348
Cooper, A. P., Parry, O. H., Lowing, B., Cole, S., & Frenk, C. 2015, MNRAS, 454, 3185
Cui, W., Murante, G., Monaco, P., et al. 2014, MNRAS, 437, 816
D'Abrusco, R., Cantiello, M., Paolillo, M., et al. 2016, ApJ, 819, L31
Deason, A. J., Belokurov, V., Evans, N. W., & Johnston, K. V. 2013, ApJ, 763, 113
DeMaio, T., Gonzalez, A. H., Zabludoff, A., et al. 2018, MNRAS, 474, 3009
Donzelli, C. J., Muriel, H., & Madrid, J. P. 2011, ApJS, 195, 15
Drinkwater, M. J., Gregg, M. D., & Colless, M. 2001, ApJ, 548, L139
Duc, P. A. 2017, in Formation and Evolution of Galaxy Outskirts, eds. A. Gil de Paz, J. H. Knapen, & J. C. Lee, IAU Symp., 321, 180
Duc, P.-A., Cuillandre, J.-C., Karabal, E., et al. 2015, MNRAS, 446, 120
Ferguson, H. C. 1989, AJ, 98, 367
Ferrarese, L., Côté, P., Cuillandre, J.-C., et al. 2012, ApJS, 200, 4
Forbes, D. A., Grillmair, C. J., Williger, G. M., Elson, R. A. W., & Brodie, J. P. 1998, MNRAS, 293, 325
Frank, K. A., Peterson, J. R., Andersson, K., Fabian, A. C., & Sanders, J. S. 2013, ApJ, 764, 46
Gonzalez, A. H., Zabludoff, A. I., & Zaritsky, D. 2005, ApJ, 618, 195
Greene, J. E., Veale, M., Ma, C.-P., et al. 2019, ApJ, 874, 66
Hartke, J., Arnaboldi, M., Gerhard, O., et al. 2018, A&A, 616, A123
Henden, N.A., Puchwein, E., & Sijacki, D. 2019, MNRAS, submitted [arXiv:1911.12367]
Hilker, M., Richtler, T., Barbosa, C. E., et al. 2018, A&A, 619, A70
Iodice, E., Capaccioli, M., Grado, A., et al. 2016, ApJ, 820, 42
Iodice, E., Spavone, M., Capaccioli, M., et al. 2017a, ApJ, 839, 21
Iodice, E., Spavone, M., Cantiello, M., et al. 2017b, ApJ, 851, 75
Iodice, E., Spavone, M., Capaccioli, M., et al. 2019a, A&A, 623, A1
Iodice, E., Sarzi, M., Bittner, A., et al. 2019b, A&A, 627, A136
Iodice, E., Spavone, M., Cattapan, A., et al. 2020, A&A, 635, A3
Jiménez-Teja, Y., Dupke, R.A., Lopes de Oliveira, R., et al. 2019, A&A, 622, A183
Jordán, A., Blakeslee, J. P., Côté, P., et al. 2007, ApJS, 169, 213
Kuijken, K. 2011, Messenger, 146, 8
La Barbera, F., Ferreras, I., de Carvalho, R. R., et al. 2012, MNRAS, 426, 2300
Longobardi, A., Arnaboldi, M., Gerhard, O., et al. 2013, A&A, 558, A42
Lucy, L. B. 1974, AJ, 79, 745
Ma, C.-P., Greene, J. E., McConnell, N., et al. 2014, ApJ, 795, 158
Mancillas, B., Duc, P.-A., Combes, F., et al. 2019, A&A, 632, A122
Melnick, J., White, S. D. M., & Hoessel, J. 1977, MNRAS, 180, 207
Merritt, A., van Dokkum, P., Abraham, R., & Zhang, J. 2016, ApJ, 830, 62
Mihos, C. 2015, IAU Gen. Assembly, 22, 2247903
Mihos, J. C., Harding, P., Feldmeier, J. J., et al. 2017, ApJ, 834, 16
Monachesi, A., Gómez, F. A., Grand, R. J. J., et al. 2019, MNRAS, 485, 2589
Munoz, R. P., Eigenthaler, P., Puzia, T. H., et al. 2015, ApJ, 813, L15
Napolitano, N. R., Arnaboldi, M., & Capaccioli, M. 2002, A&A, 383, 791
Napolitano, N. R., Pannella, M., Arnaboldi, M., et al. 2003, ApJ, 594, 172
Oser, L., Ostriker, J. P., Naab, T., Johansson, P. H., & Burkert, A. 2010, ApJ, 725, 2312
Paolillo, M., Fabbiano, G., Peres, G., & Kim, D.-W. 2002, ApJ, 565, 883
Peng, Y.-J., Lilly, S. J., Kovač, K., et al. 2010, ApJ, 721, 193
Pillepich, A., Nelson, D., Hernquist, L., et al. 2018, MNRAS, 475, 648
Pinna, F., Falcón-Barroso, J., Martig, M., et al. 2019a, A&A, 625, A95
Pinna, F., Falcón-Barroso, J., Martig, M., et al. 2019b, A&A, 623, A19
Pop, A.-R., Pillepich, A., Amorisco, N. C., & Hernquist, L. 2018, MNRAS, 480, 1715
Pota, V., Napolitano, N. R., Hilker, M., et al. 2018, MNRAS, 481, 1744
Prole, D. J., Hilker, M., van der Burg, R. F. J., et al. 2019, MNRAS, 484, 4865
Raj, M. A., Iodice, E., Napolitano, N. R., et al. 2019, A&A, 628, A4
Raj, M. A., Iodice, E., Napolitano, N. R., et al. 2020, A&A, submitted
Richardson, W. H. 1972, J. Opt. Soc. Am. (1917–1983), *62*, 55
Rudick, C. S., Mihos, J. C., & McBride, C. K. 2011, ApJ, 732, 48
Sarzi, M., Iodice, E., Coccato, L., et al. 2018, A&A, 616, A121
Scharf, C. A., Zurek, D. R., & Bureau, M. 2005, ApJ, 633, 154
Schipani, P., Noethe, L., Arcidiacono, C., et al. 2012, J. Opt. Soc. Am. A, 29, 1359
Scott, N., Eftekhari, F. S., Peletier, R. F., et al. 2020, MNRAS, submitted
Seigar, M. S., Graham, A. W., & Jerjen, H. 2007, MNRAS, 378, 1575
Serra, P., de Blok, W. J. G., Bryan, G. L., et al. 2016, Proceedings of MeerKAT Science: On the Pathway to the SKA. 25–27 May, 2016 Stellenbosch, South Africa (MeerKAT2016), Online at https://pos.sissa.it/cgi-bin/reader/conf.cgi?confid=277,id.8,8
Sérsic, J. L. 1963, Boletin de la Asociacion Argentina de Astronomia La Plata Argentina, 6, 41
Sheardown, A., Roediger, E., Su, Y., et al. 2018, ApJ, 865, 118
Spavone, M., Capaccioli, M., Napolitano, N. R., et al. 2017, A&A, 603, A38
Spavone, M., Iodice, E., Capaccioli, M., et al. 2018, ApJ, 864, 149
Spiniello, C., Napolitano, N. R., Arnaboldi, M., et al. 2018, MNRAS, 477, 1880
Tacchella, S., Diemer, B., Hernquist, L., et al. 2019, MNRAS, 487, 5416
Thuan, T. X., & Kormendy, J. 1977, PASP, 89, 466
Trujillo, I., & Fliri, J. 2016, ApJ, 823, 123
van der Kruit, P. C., & Freeman, K. C. 2011, ARA&A, 49, 301
van Dokkum, P. G., Abraham, R., & Merritt, A. 2014, ApJ, 782, L24
Veale, M., Ma, C.-P., Greene, J. E., et al. 2018, MNRAS, 473, 5446
Venhola, A., Peletier, R., Laurikainen, E., et al. 2017, A&A, 608, A142
Venhola, A., Peletier, R., Laurikainen, E., et al. 2018, A&A, 620, A165
Zabel, N., Davis, T. A., Smith, M. W. L., et al. 2019, MNRAS, 483, 2251

Appendix A: Results of multi-component fits

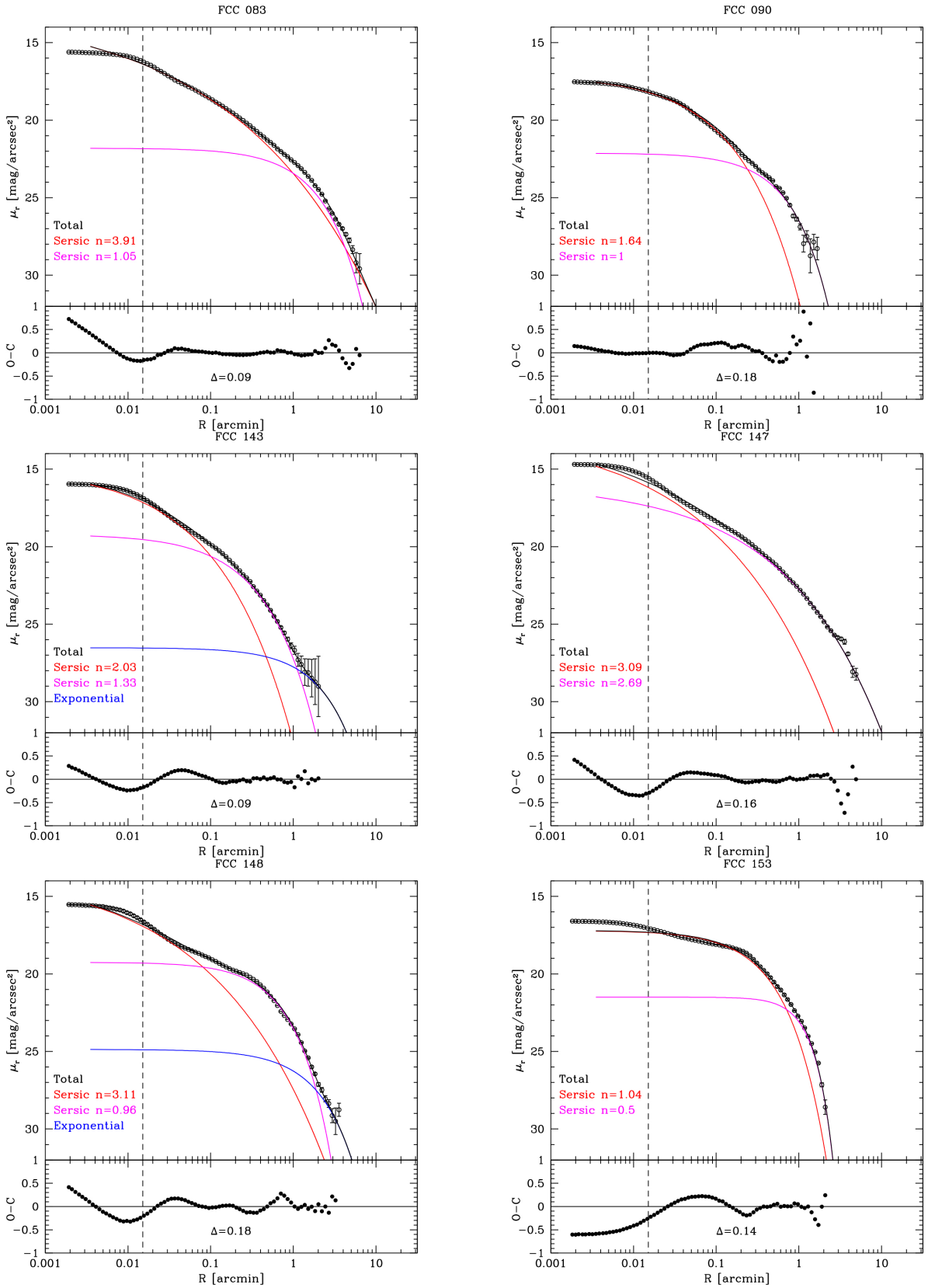

Fig. A.1. *Top panels*: deconvolved VST r-band profiles of ETGs in FDS plotted on a logarithmic scale. The blue line indicates a fit to the outer regions. The red and magenta lines indicate a fit to the inner and middle regions with a Sérsic profile, and the black line indicates the sum of the components from each fit. The dotted line indicates the core of the galaxy, which was excluded in the fit. *Bottom panels*: Δ rms scatter (see text for details).

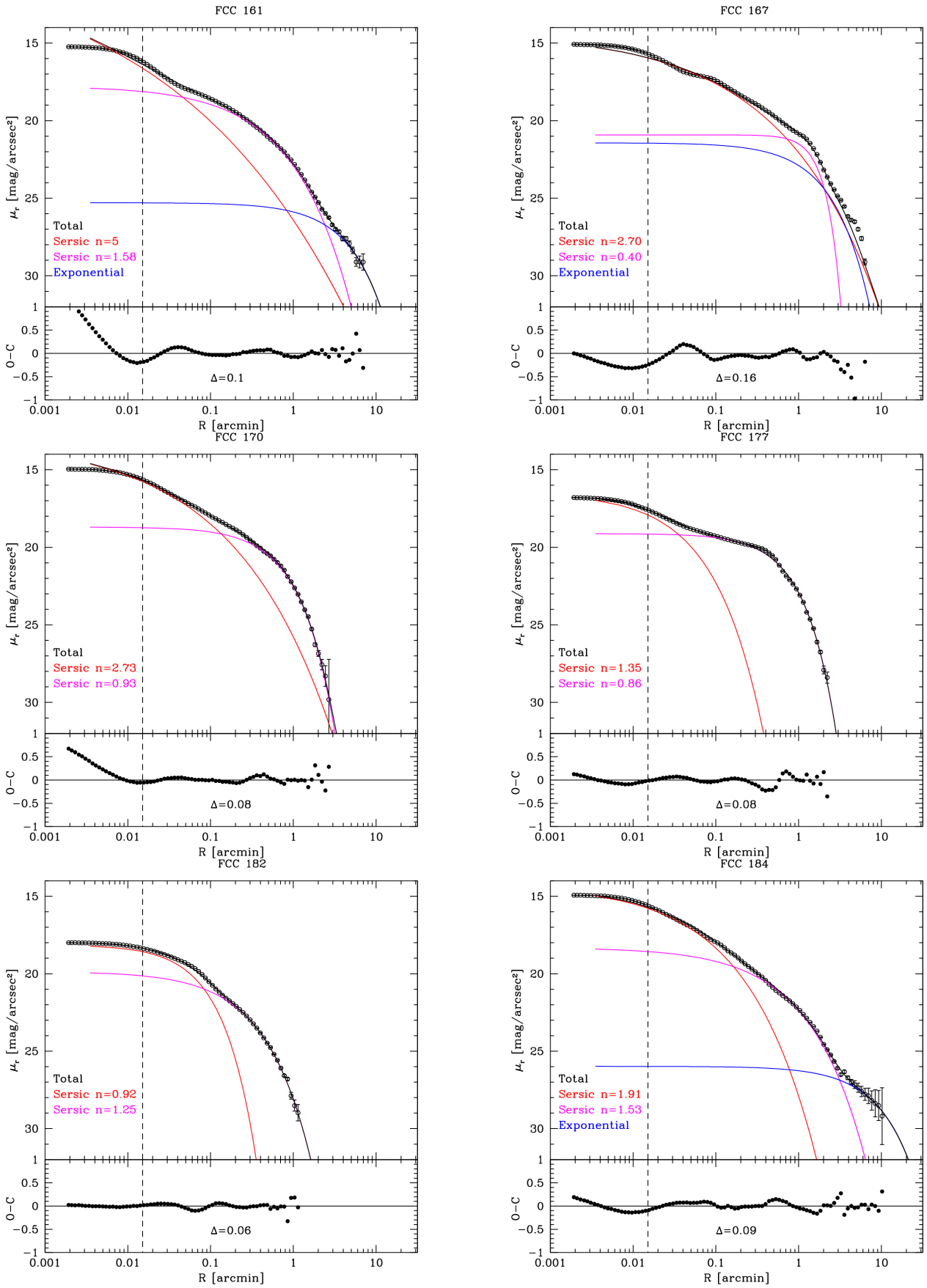

Fig. A.1. continued.

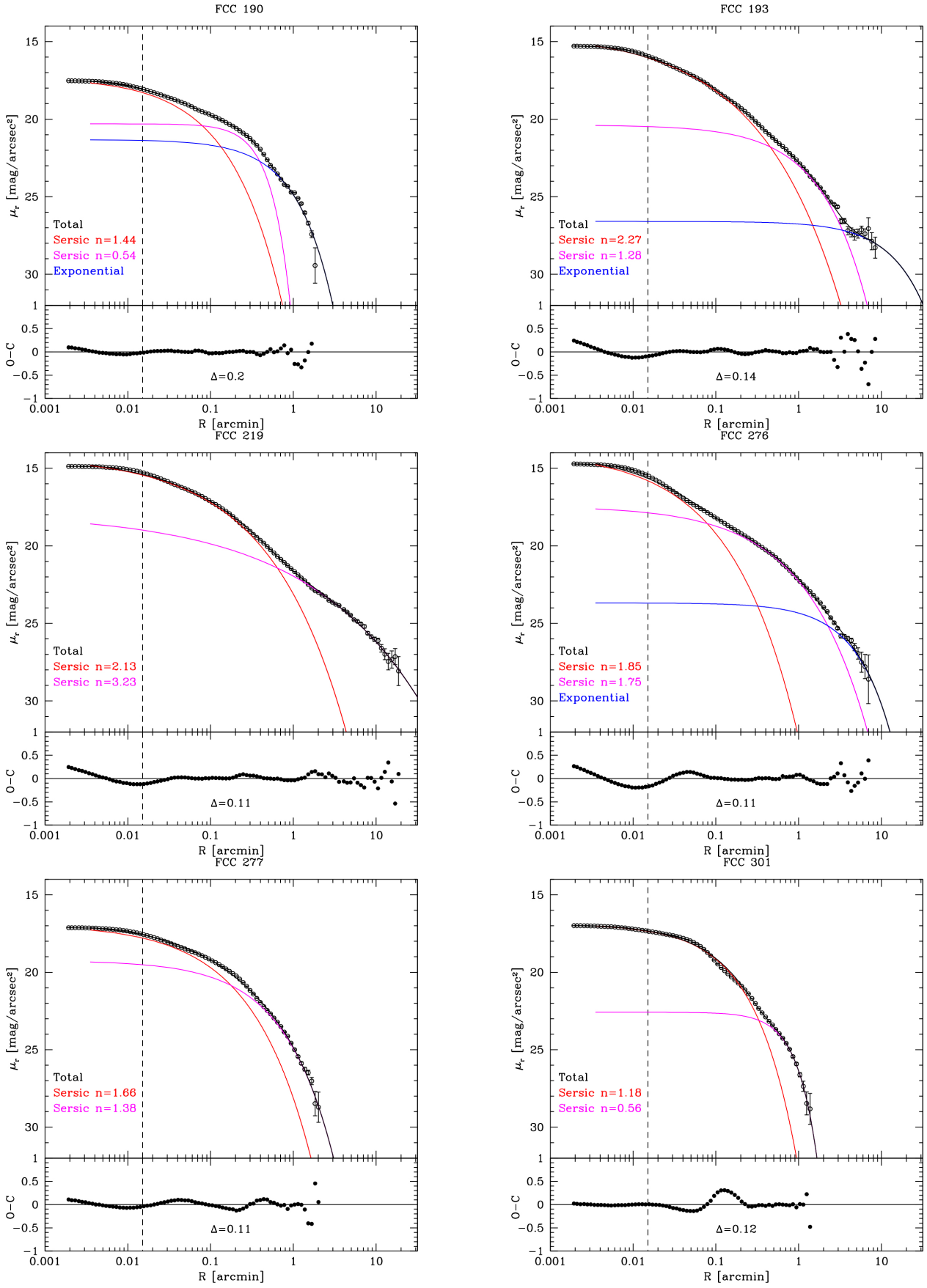

Fig. A.1. continued.

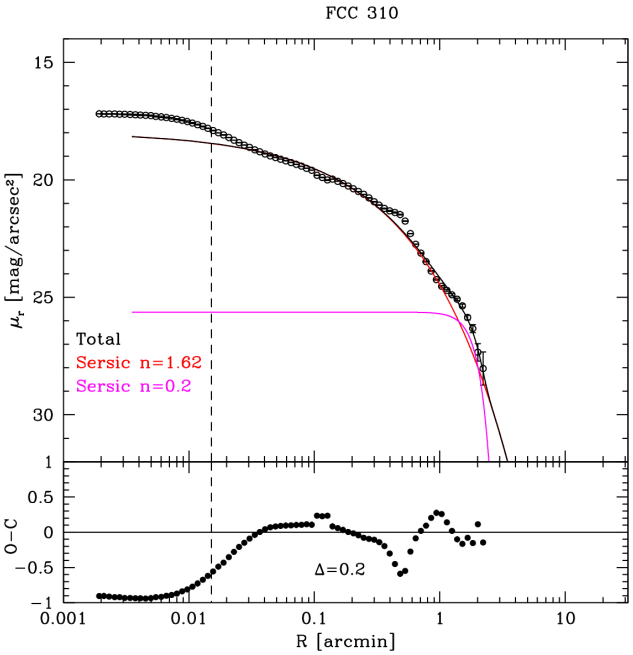

Fig. A.1. continued.